

# Aeroelastic instability of a flexible plate in a uniform flow

Christophe Eloy,\* Romain Lagrange, Claire Souilliez, and Lionel Schouveiler  
 IRPHE, CNRS & Aix-Marseille Université, 49 rue Joliot-Curie, 13013 Marseille, France  
 (Dated: April 4, 2008)

The flutter instability of a flexible plate immersed in an axial flow is experimentally investigated. This instability is similar to flag flutter and results from the competition between destabilizing pressure forces and stabilizing bending stiffness. The instability threshold is measured as a function of the experimental parameters (plate size and aspect ratio) and compared to different theoretical predictions.

PACS numbers: 46.40.Ff, 46.40.Jj, 47.15.ki, 47.20.Cq

The flutter of a flexible plate immersed in an axial flow is a canonical example of flow-induced vibrations. This instability can be experienced in everyday life when one observes a flag flapping in the wind. Because this phenomenon appears in many applications (paper industry, airfoil flutter, snoring), it has motivated a large literature which has been recently reviewed [1]. This instability can be regarded as a competition between fluid forces and elasticity. Indeed, as soon as the plate experiences a small lateral deflection, a destabilizing pressure jump appears across the plate, while the bending stiffness tends to bring the plate back to the planar state.

This system can be studied by restricting the analysis to one-dimensional flutter modes as observed in most experiments. In this case, the plate motion obeys the Euler-Bernoulli beam equation with additional pressure forces which are calculated by assuming a potential flow. As a first approach, the plate can be supposed to be infinite in both directions [2] to calculate the flow. In other theoretical studies, the plate length  $L$  (or chord) takes a finite value while two asymptotic limits are considered for its span  $H$ . If  $H \ll L$ , the fluid forces can be calculated using the Lighthill's slender body theory [3, 4] and if  $H \gg L$  the problem can be treated as two-dimensional [5, 6, 7, 8]. In this latter case, the flow is entirely described by point-vortices which are distributed within the plate and possibly in its wake. It is known from airfoil theory that this problem does not admit a unique solution (intrinsically because the Laplace equation has to be solved on an open domain). This non-unicity can be treated by two approaches [5]: one can either consider a zero total circulation around the plate and thus no vorticity in the wake, or the circulation can be prescribed by the Kutta condition applied at the trailing edge of the plate [9]. This latter condition imposes advected vortices in the wake which makes this model more physical for this flag-type instability. Note that this shed vorticity can equivalently be regarded as the consequence of the Kelvin's circulation theorem.

Using these two-dimensional flow models, a stability analysis can be carried out that allows to predict the critical velocity for plate flutter. These theories have been compiled by Watanabe *et al.* [6] and compared with

existing experimental data [3, 7]. Remarkably all these theories predict approximately the same critical velocities but strongly underestimate the measured thresholds. In other words, the plate appears systematically more stable than predicted by a two-dimensional approximation. This discrepancy has motivated the recent study of Eloy *et al.* [10] in which the finite plate span is explicitly taken into account in the analysis. The present paper aims at comparing their predictions with experimental measurements in which the effect of the plate aspect ratio  $H/L$  is extensively investigated.

As shown in Fig. 1, we consider a flexible plate of span  $H$  and length  $L$ , lying in the vertical plane ( $Oxy$ ) and immersed in an axial flow of velocity  $U$ . Its flexural rigidity is given by  $D = Eh^3/12(1 - \nu^2)$ , where  $E$  is the Young's modulus,  $h$  the plate thickness and  $\nu$  its Poisson's ratio. For small lateral deflections  $z(x, t)$ , the plate motion is driven by the linearized Euler-Bernoulli equation

$$m \partial_t^2 z + D \partial_x^4 z + \langle [p] \rangle = 0, \quad (1)$$

where  $m$  is the mass per unit surface of the plate,  $[p](x, y, t)$  is the pressure jump across the plate and the notation  $\langle . \rangle$  stands for the average along the span  $H$ . Equation (1) is valid in the limit of an inviscid fluid and for a material of negligible visco-elastic damping. In addition the deflection  $z$  satisfies clamped boundary conditions at the leading edge:  $z(0) = \partial_x z(0) = 0$  and free boundary conditions at the trailing edge:  $\partial_x^2 z(L) = \partial_x^3 z(L) = 0$ .

Assuming an inviscid flow, the perturbation velocity can be fully described by the vorticity distribution in the flow. Vortex-lines are located in the plate and in its wake as sketched on Fig. 1(b). The pressure jump across the plate only depends on the  $y$ -component of the vorticity  $\gamma(x, y, t)$  through the unsteady Bernoulli equation

$$\partial_x [p] = \rho U (\partial_t + U \partial_x) \gamma, \quad (2)$$

where  $\rho$  is the fluid density. As seen from this equation a vorticity distribution of the form  $\gamma_0(y) \exp[i(kx - \omega t)]$  with wave velocity  $\omega/k = U$  is compatible with a zero pressure jump and is indeed the distribution of vorticity in the wake.

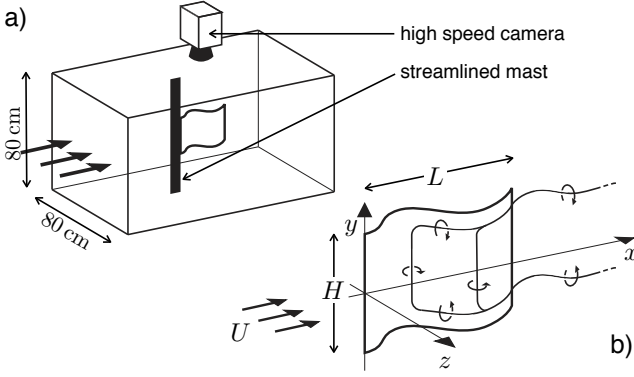


FIG. 1: Sketch of the experimental setup (a); and plate subject to the one-dimensional deflection  $z(x, t)$  (b).

In order to couple the vorticity distribution  $\gamma$  to the plate deflection  $z$ , a kinematic condition is enforced on the plate surface which can be written as

$$\oint \langle \gamma(\xi) \rangle K(x - \xi) d\xi = (\partial_t + U \partial_x) z = w(x, t), \quad (3)$$

where  $\xi$  is a dummy variable in place of  $x$ ,  $w$  is the normal plate velocity in the fluid reference frame and the letter  $C$  across the integral sign indicates that the Cauchy principal value should be taken. Since this inverse problem can have non-unique solutions, the Kutta condition is also used at the trailing edge i.e.  $[p](L) = 0$ . The kernel  $K$  in Eq. (3) expresses the influence of a vertical vorticity line located in  $\xi$  on the  $z$ -component of the fluid velocity in  $x$ . For an infinite span, the azimuthal velocity of a point-vortex in 2D yields the kernel  $K(X) = 1/2\pi X$  used in 2D models [5]. For an asymptotically small  $H$  the Lighthill's slender body theory is equivalent to taking  $K(X) = \text{sgn}(X)/\pi H$ . In Eloy *et al.* [10], we have shown that an approximate kernel can be used for any  $H$

$$K(X) = \frac{1}{2\pi X} + \left( \frac{1}{\pi H} - \frac{1/\pi - 1/8}{H + |X|} \right) \text{sgn}(X), \quad (4)$$

which is constructed to have the correct asymptotic behavior for small and large  $H$ .

To address the stability of this fluid-structure coupling, the full linearity of this problem is used and Galerkin decomposition can be assumed for the deflection:  $z(x, t) = \sum_n z_n(x) \exp(i\omega t)$ . For a given Galerkin mode, one has then to invert Eq. (3) and inject the solution in Eq. (2) to find the corresponding pressure jump  $\langle [p_n] \rangle \exp(i\omega t)$ . The partial differential equation (1) is then reduced to an eigenvalue problem for the complex frequency  $\omega$  whose eigenmodes correspond to the instability modes. For small flow velocity, all modes are stable (i.e. their complex frequencies  $\omega$  have a positive imaginary part). When  $U$  is larger than a critical flow velocity  $U_c$ , one of the instability modes eventually becomes unstable.

Using  $L$  and  $L/U$  as characteristic length and time, the system parameters are reduced to three dimensionless numbers: the reduced velocity  $U^*$ , the mass ratio  $M^*$  and the aspect ratio  $H^*$  given by

$$U^* = LU \sqrt{m/D}, \quad M^* = \rho L/m, \quad H^* = H/L. \quad (5)$$

In this dimensionless form, the present theory (see Ref. 10 for details) allows to predict the critical velocity  $U_c^*(M^*, H^*)$  and the dimensionless mode frequencies  $\omega^* = \omega L/U$ . Note however that the pressure singularity at the leading edge has been artificially suppressed in this analysis in such a way that that, in the limit of infinite  $H^*$ , the results of the 2D theory of Kornecki *et al.* [5] are not exactly recovered (their results have been recalculated in the present paper with better computer accuracy to allow comparisons).

As sketched in Fig. 1(a) experiments were performed in a low-turbulence closed wind tunnel of  $80 \times 80 \text{ cm}^2$  cross section. The wind velocity  $U$  could be varied continuously up to  $65 \text{ m s}^{-1}$  and was measured with a Pitot tube. The plates were clamped in a streamlined mast crossing the wind tunnel vertically. To ensure that the mast had negligible effects on the instability, two masts of different cross section were used (mast 1: thickness  $\times$  chord =  $4 \text{ mm} \times 20 \text{ mm}$ ; mast 2:  $9 \text{ mm} \times 43 \text{ mm}$ ). Plates were cut in Mylar sheets of mass per unit area  $m = 140 \text{ g m}^{-2}$  and flexural rigidity  $D = 0.48 \times 10^{-3} \text{ N m}$ . To estimate  $D$ , the deflection due to gravity was measured for horizontally clamped Mylar strips of various lengths.

In all experiments presented in this paper, the same protocol has been followed. The plate is clamped in the mast and the flow velocity is slowly increased starting from zero. At small velocities the plate appears stable, i.e. stationary and aligned with the flow. Eventually, for a critical flow velocity  $U_c^*$ , the plate flutters spontaneously with a large amplitude and a well-defined frequency. Then the flow velocity is slowly decreased in small decrements until the plate returns to its stable state again at the critical velocity  $U_d^*$  as illustrated in Fig. 2.

Visualizations were carried out through the top wall of the wind tunnel with a high speed video camera aligned with the  $y$ -axis (see Fig. 1a). In the present experiments, the camera was operating at 300 Hz with a  $512 \times 512$  pixel resolution and the exposure time was varied between 300 and  $1500 \mu\text{s}$ . The camera visualizations are used to extract the mode amplitude  $A$  and its angular frequency  $\omega^*$ . This is done by detecting for each snapshot the plate deflection at  $3/4$  of the total plate length.

The mode amplitude  $A$  is plotted in Fig. 2 as a function of the reduced velocity and exhibits a hysteretic behavior. This has been observed in all experiments with sufficiently large aspect ratio ( $H^* \gtrsim 1$ ). This hysteresis together with the large mode amplitude observed at threshold evokes a subcritical instability bifurcation as recently suggested by numerical results [11]. However, in other nonlinear numerical models [12, 13], the bifurcation

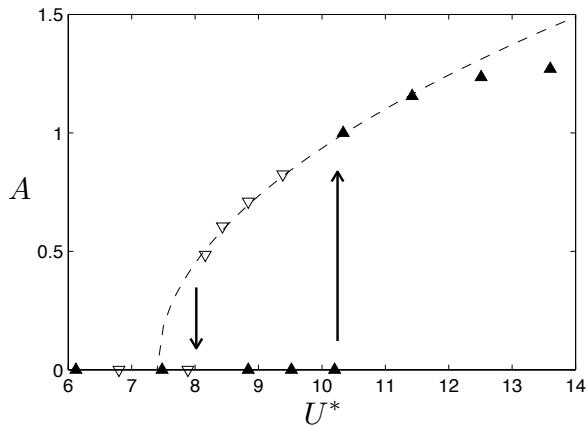


FIG. 2: Mode amplitude  $A$  (in arbitrary units) as a function of the reduced velocity  $U^*$ . Amplitude is plotted as filled triangles when velocity is increased and open triangles when it is decreased. The experimental parameters are  $H^* = 1$  and  $M^* = 0.6$ . The instability exhibits a strong hysteresis with  $U_c^* = 10.3$  and  $U_d^* = 8$ . However, the amplitudes are well fitted by the square-root law  $A = 58(U^* - 7.4)^{1/2}$  (dashed line) suggesting a supercritical bifurcation.

is supercritical. Figure 2 shows that the amplitudes near threshold can be reasonably well fitted with a square-root law giving evidence that the bifurcation could indeed be supercritical and that the observed hysteresis could just be an artifact as discussed below.

The critical velocities  $U_c^*$  and  $U_d^*$  are plotted in Fig. 3 as a function of the aspect ratio  $H^*$  and the mass ratio  $M^*$ . First the plate span is varied keeping its length constant. This allows to vary the aspect ratio without changing the other parameters. As expected from slender body theory, the critical velocity tends to decrease as aspect ratio is increased. From Fig. 3(a) two regimes can be distinguished. For small aspect ratio ( $H^* \lesssim 1$ ), the measured critical velocities are well predicted by the linear stability analysis and the hysteresis is very small. For larger aspect ratio ( $H^* \gtrsim 1$ ) the hysteresis greatly increases as well as experimental scatter and the linear stability analysis tends to underestimate the critical velocity  $U_c^*$ . Moreover, this threshold seems to slightly increase for  $1 < H^* < 3$  contrarily to the decreasing threshold  $U_d^*$  and contrarily to the predictions.

In Fig. 3(b), the aspect ratio has been kept constant ( $H^* = 1$ ) by varying by the same factor the plate length and span. The measured critical velocity  $U_c^*$  is compared to the theoretical predictions of the present analysis [10] and the 2D model of Kornecki *et al.* [5]. In the present analysis, the finiteness of the span is taken into account leading to a smaller destabilizing term  $\langle [p] \rangle$  in Eq. (1) compared to the 2D model and thus a better prediction of the instability threshold. Both models allow to predict different instability modes as  $M^*$  is increased as illustrated by the different lobes in Fig. 3(b). If modes are numbered by order of ascending frequencies, the mode

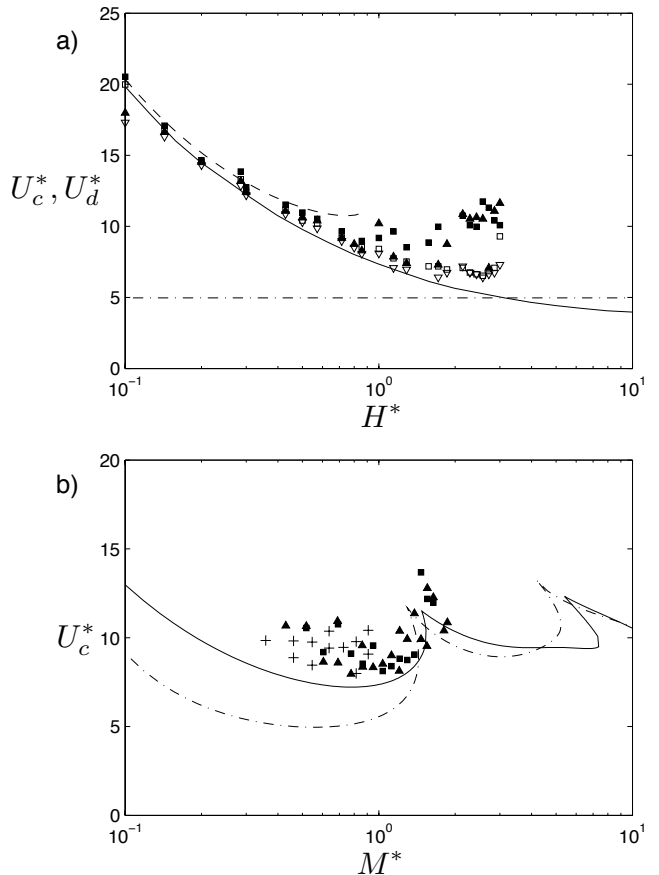


FIG. 3: Critical velocities  $U_c^*$  and  $U_d^*$  as a function of the aspect ratio  $H^*$  for  $M^* = 0.6$  (a) and as a function of the mass ratio  $M^*$  for  $H^* = 1$  (b). Filled squares and triangles correspond to measured  $U_c^*$  for the masts 1 and 2 respectively and the same open symbols refer to  $U_d^*$ . Crosses correspond to the experiments of Ref. 7 for  $0.6 < H^* < 1.5$ . The solid line is the 3D theory of Ref. 10 for same the parameters, the dashed line is the slender body theory (similarly to Ref. 4) and the dash-dotted line corresponds to the 2D theory with circulation (same as Ref. 5 with better computer accuracy).

two is observed for the smallest mass ratios ( $M^* \lesssim 1.5$ ). This single-neck mode is pictured in Fig. 4(a,b). For larger mass ratios ( $1.5 \lesssim M^* \lesssim 5$ ), the mode three, a double-neck mode, is the first unstable one as illustrated in Fig. 4(c,d). Note that the mode one (the mode with the smallest frequency) is never unstable for a clamped-free plate as it is discussed in refs. [8, 10]. For larger mass ratios ( $M^* \gtrsim 5$ ), one would observe higher order modes (but in such experiments, plates are so thin that gravity makes them twist). In other words, as  $M^*$  increases, the typical mode wavelength  $\lambda$  is a smaller fraction of the plate length  $L$  and therefore if the aspect ratio is kept constant,  $H/\lambda$  increases. This span to wavelength ratio has to be large for a 2D theory to be valid and This explain why the difference between the 2D and 3D theoretical approaches reduces as  $M^*$  increases in Fig. 3(b).

In Fig. 4(a,c), superimposed views of the plate

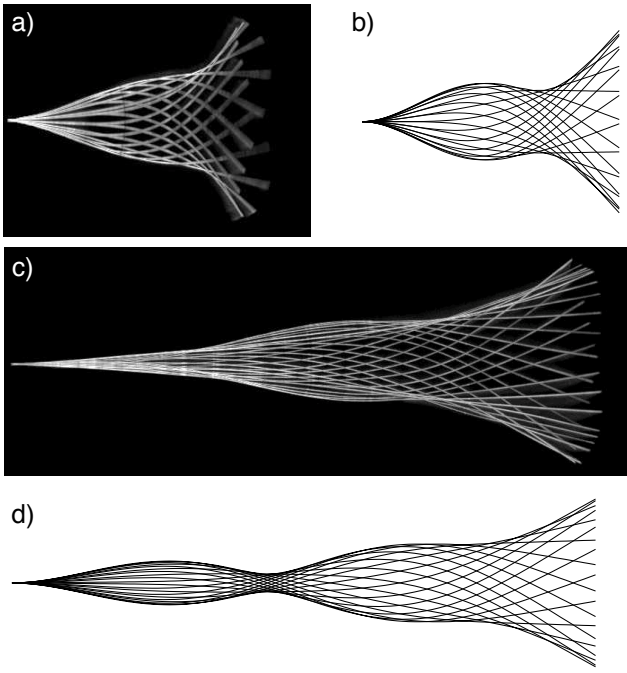


FIG. 4: Superimposed views of the flutter modes for two plates of same aspect ratio  $H^* = 1$  but with different sizes [ $M^* = 0.74$  for (a) and (b),  $M^* = 1.94$  for (c) and (d)]. These amplitudes are obtained at threshold and the measured frequencies are  $\omega^* = 1.82$  for  $U_c^* = 8.1$  (a) and  $\omega^* = 2.5$  for  $U_c^* = 10.9$  (c). The experimental snapshots are compared with the modes predicted by the present linear stability analysis (with arbitrary amplitude):  $\omega^* = 2.4$  for  $U_c^* = 7.2$  (b) and  $\omega^* = 3.7$  for  $U_c^* = 10.4$  (d).

recorded with the camera during one flutter period are shown. These visualizations were carried out at the instability threshold  $U_c^*$  for plates of same aspect ratio  $H^* = 1$  but for two different mass ratios. As predicted by the analysis, different modes are observed as  $M^*$  varies. From these data, the mode shapes and their frequencies can be compared to the theoretical predictions for the same parameters. However nonlinear effects are probably important given the large amplitude observed at threshold and the agreement with the results of the linear stability analysis are only qualitative.

In the experiments with large aspect ratio  $H^* > 1$ , the flutter mode is no longer purely one-dimensional as the top corner flutters with a larger amplitude than the rest of the plate. Moreover, in some experiments with a very large aspect ratio  $H^* = 4$  and for flow velocity just below threshold, the same top corner flutters while the rest of the plate is still motionless. This indicates that the Euler-Bernoulli beam equation for the plate is no longer valid and one should use the nonlinear Föppl-von Kármán equations as soon as the deflection along the span is of the order of the plate thickness. The reasons for the two-dimensionality of the plate deflection are twofold. First, the pressure field over the plate is non

uniform along the span and exhibit a maximum at mid-span and zeros at the plate edges. Second, the gravity field induces a non trivial stress tensor in the plate that induces compression at the top corner and tension at the bottom corner. Since tension has a stabilizing effect, this may explain why the top corner is the most unstable position. Finally, one should note that bending along the span acts as a stiffening effect (because Gauss curvature is energetically costly) and therefore it has a stabilizing effect on the flutter instability.

As explained above, the leading-edge pressure singularity is not properly taken into account in the present analysis (mostly because it greatly simplifies the problem). This explains why the solid curve in Fig. 3(a) does not tend for large  $H^*$  to the 2D limit represented by the dash-dotted line. If a proper full three-dimensional stability analysis was carried out, the critical curve  $U_c^*(H^*)$  would be slightly above the solid line of Fig. 3(a) in order to converge to the 2D limit. In this case, the theoretical threshold would be even closer to the open symbols representing the descending threshold  $U_d^*$ . This is another argument for a supercritical bifurcation. Indeed, the instability could be delayed and the measured  $U_c^*$  higher than  $U_d^*$  because of small imperfections of the flow (due to the wind tunnel or the wake of the mast) driving a small two-dimensional plate vibration or deflection and thus stiffening the system as exposed above.

The authors acknowledge support from the French ANR (No. ANR-06-JCJC-0087).

---

\* Electronic address: eloy@irphe.univ-mrs.fr

- [1] M. P. Païdoussis, *Fluid-Structure Interactions: Slender Structures And Axial Flow* (Elsevier Academic Press, London, 2004).
- [2] M. Shelley, N. Vandenberghe, and J. Zhang, *Phys. Rev. Lett.* **94**, 094302 (2005).
- [3] S. K. Datta and W. G. Gottenberg, *J. Appl. Mech.* **75**, 195 (1975).
- [4] C. Lemaitre, P. Hémon, and E. de Langre, *J. Fluids Struct.* **20**, 913 (2005).
- [5] A. Kornecki, E. H. Dowell, and J. O'Brien, *J. Sound Vib.* **47**, 163 (1976).
- [6] Y. Watanabe, K. Isogai, S. Suzuki, and Sugihara, *J. Fluids Struct.* **16**, 543 (2002).
- [7] L. Huang, *J. Fluids Struct.* **9**, 127 (1995).
- [8] C. Q. Guo and M. P. Païdoussis, *J. Appl. Mech.* **67**, 171 (2000).
- [9] T. Theodorsen, *Tech. Rep. TR-496*, NACA (1935).
- [10] C. Eloy, C. Souilliez, and L. Schouveiler, *J. Fluids Struct.* **23**, 904 (2007).
- [11] S. Alben and M. J. Shelley, *Phys. Rev. Lett.* **100**, 074301 (2008).
- [12] D. M. Tang, H. Yamamoto, and E. H. Dowell, *J. Fluids Struct.* **17**, 225 (2003).
- [13] Y. Yadykin, V. Tenetov, and D. Levin, *J. Fluids Struct.* **15**, 1167 (2001).